Influence of Transceiver Array Aperture Size on Electromagnetic Linear Inverse Scattering From 2-D Objects Embedded in Planarly Multilayered Media

Sijia Ma, Kemeng Tao, and Feng Han, *Senior Member, IEEE*

***Abstract*— This article studies the effect of transceiver array aperture size on the inversion ability of the linear integral equation-based solver for the electromagnetic (EM) reconstruction of 2-D scatterers embedded inside a planarly multilayered medium. The investigation is performed in three steps. First, we derive the analytical relationship between the spectra of the scattered electric fields at the receiver array and the reconstructable 2-D scatterer spectrum, which is composed of four different spectral components. This is completely different from the single spectral component for the 2-D scatterer directly placed in a homogeneous subsurface region. Second, the singular value decomposition (SVD) is adopted to compute the discretized integral operator's right-singular function whose spectrum can also reflect the reconstructable 2-D scatterer spectrum but with the wave attenuation and evanescent mode contribution taken into account. The obtained spectrum shows a "bandstop" feature in the vertical direction with a decrease in the transceiver array aperture size, which is totally different from the "bandpass" feature for the 2-D scatterer embedded in the homogeneous subsurface region. Third, the features of the reconstructable spectrum of the 2-D scatterer embedded inside a planarly multilayered medium, especially the "bandstop" feature, are validated in a series of numerical experiments.**

***Index Terms*— Electromagnetic (EM) inverse scattering, full-wave inversion (FWI), multilayered media, transceiver array aperture size.**

I. Introduction

ELECTROMAGNETIC (EM) inverse scattering, sometimes also called EM full-wave inversion (FWI), is to infer the model parameters of unknown objects from the scattered field data recorded at the receiver array [1]. The related research in the early days was only focused on the reconstruction of simple models with small electrical sizes and inversion of an extremely limited number of model parameters. For example, in [2] and [3], only one 1-D constitutive parameters of inhomogeneous scatterers were reconstructed by simple alternative iteration methods in the time domain and the frequency domain, respectively. In later research, more sophisticated iterative methods are proposed and used to deal with complicated EM scattering problems, e.g., 2-D or 3-D inhomogeneous and anisotropic scatterers with large electrical dimensions [4], [5]. The commonly used approaches can be roughly divided into two categories, the integral equation (IE)-based and differential equation (DE)-based ones, according to the forward scattering solvers employed in the alternative iterations. Typical IE-based approaches include Born iterative method (BIM) [6], distorted BIM (DBIM) [7], variational BIM (VBIM) [8], contrast source inversion (CSI) [9], [10], and subspace optimization method (SOM) [11], as well as some hybrid ones [12], [13]. They have wide applications in both academic researches [14], [15], [16], [17] and engineering problems, e.g., underground abnormal object inspection [18] and human tissue anatomy [19]. These IE-based inverse scattering methods have the intrinsic merit that the inversion domain can tightly wrap the unknown objects and thus the degree of freedom in inversion is limited. However, because the inversion domain and the transceivers are linked by Green's functions, the background medium must be regular (e.g., homogeneous, planarly layered, etc.) to guarantee their computability. The DE-based EM FWI uses DEs, e.g., Helmholtz equation, to describe wave propagation and thus can adapt to any irregular background media. Commonly used inversion algorithms include the nonlinear conjugate gradient (NLCG) method [20], the quasi-Newton (QN) method [21], and the Gauss–Newton (GN) method [22]. And they have been successfully applied to both 2-D [23] and 3-D [24] geophysical inversions.

Most of these research works are focused on the improvement of the FWI methods and their applications to engineering problems, e.g., microwave imaging and geophysical exploration. Another important research branch in EM wave imaging and inversion that has drawn the intensive attention of researchers in the past decades is the influence of the transceiver array layout on the inversion performance. It is mainly achieved by quantitatively analyzing the relationship

Manuscript received 11 December 2023; revised 14 February 2024; accepted 20 March 2024. Date of publication 22 March 2024; date of current version 2 April 2024. This work was supported by the National Natural Science Foundation of China under Grant 62271428. *(Corresponding author: Feng Han.)*

Sijia Ma and Kemeng Tao are with the Institute of Electromagnetics and Acoustics and Key Laboratory of Electromagnetic Wave Science and Detection Technology, Xiamen University, Xiamen 361005, China.

Feng Han is with the School of Computing and Information Technology, Great Bay University, Guangdong 523000, China, and also with Institute of Electromagnetics and Acoustics, Xiamen University, Xiamen 361005, China (e-mail: feng.han@gbu.edu.cn; feng.han@xmu.edu.cn).

Digital Object Identifier 10.1109/TGRS.2024.3380740

between the reconstructable spectrum bandwidth of subsurface 2-D scatterers and the transceiver array aperture size [25]. By analytically correlating the reconstructable scatterer spectrum with the scattered field spectrum at the receiver array via linearizing the integration equation and a series of Fourier transforms, researchers first acquire the reconstructable spectrum range through guaranteeing the valid wavenumbers of both incident and scattered waves. Then, for more practical EM scattering and inverse scattering scenarios with the wave attenuation and evanescent mode contribution considered, the singular value decomposition (SVD) is adopted to numerically compute the discretized integral operator's right-singular function whose spectrum also represents the scatterer reconstructable spectrum. Finally, FWI of scatterers with low contrasts is implemented in numerical examples to verify the theoretical analysis and SVD results. This complete set of methods was later also used to analyze and validate the influence of transceiver spatial offsets [26], frequency hopping step [27], [28], and the real antenna radiation pattern [29] on the 2-D reconstructable spectrum of the subsurface scatterers. However, in most of these works, the background medium is assumed to be a homogeneous model or a simple half-space model, which is far from the real situations in many EM inversion applications.

In this article, we extend the previous works to a more realistic EM scattering scenario for which the 2-D scatterers are placed inside a planarly multilayered medium. Compared with previous works, this work has the following new contributions.

1) A completely different spectral relationship between scattered electric fields at the receiver array and the 2-D scatterers is derived based on the multilayered medium Green's functions. The reconstructable scatterer spectrum is weighted by a group of coefficients that depend on the multiple reflections and transmissions in multiple layer boundaries.
2) The computed reconstructable spectrum is not single. Instead, it is composed of four different components that correspond to four different incident and scattered EM wave propagation pictures inside the inversion domain, which actually is caused by multiple reflections and transmissions in multiple layer boundaries.
3) The obtained overall reconstructable spectrum shows a "lowpass" feature in the horizontal direction with the decrease in the array aperture size, which is the same as that for the half-space model given in the previous work. However, in the vertical direction, the overall reconstructable spectrum shows a "bandstop" feature instead of the "bandpass" feature.
4) The "bandstop" feature of the overall spectrum is successfully validated by numerical examples based on Born approximation.

The organization of this article is as follows. In Section II, the analytical relationship between the scattered electric field spectrum at the receiver array and the spectrum of the 2-D scatterer placed inside a planarly multilayered medium is derived. Then, the influence of the transceiver array aperture size on the bandwidth of the reconstructable spectrum is analyzed theoretically in Section III, analyzed by SVD in Section IV, and validated by numerical experiments in Section V, respectively. Finally, in Section VI, the conclusion and the possible future work are presented.

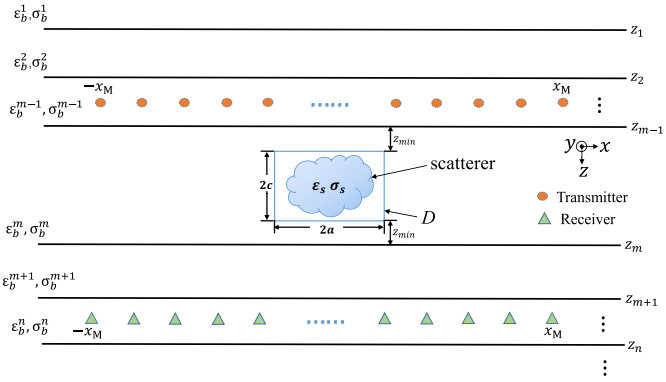

Fig. 1. Configuration of the 2-D EM inverse scattering from inhomogeneous scatterers embedded in the mth layer of a multilayered medium. The inversion domain D enclosing the scatterer has the dimensions of $2a \times 2c$.

II. Linear Inverse Scattering From 2-D Objects Embedded in a Planarly Multilayered Medium

As shown in Fig. 1, the background 2-D space is separated by a series of parallel planar interfaces located at $z = z_1, z_2, \ldots, z_n$. The 2-D scatterer is completely embedded inside the mth layer which has the complex relative permittivity $\epsilon_b = \varepsilon_b^m + (\sigma_b^m / j\omega\varepsilon_0)$ and the permeability μ_0. The inhomogeneous scatterer with the spatially varying relative permittivity $\varepsilon_s(\boldsymbol{\rho})$ and conductivity $\sigma_s(\boldsymbol{\rho})$ is placed inside the rectangular inversion domain D with the dimensions of $2a \times 2c$. The upper surface of the domain D is $z_{\min}$ away from the interface $z = z_{m-1}$ and the lower surface is also $z_{\min}$ away from the interface $z = z_m$. Both the transmitter array located at $z = z_s$ and the receiver array located at $z = z_r$ have the horizontal sizes $2x_M$. Note that they can be placed inside the same background layer or in different layers. In addition, one should note that the inversion domain D is intentionally placed symmetrically in the vertical $\hat{z}$-direction inside the mth background layer. Such a configuration is to guarantee that the transceiver arrays have the same aperture sizes with respect to the inversion domain when they are located on the same side or two different sides of the inversion domain if their true length $2x_M$ values are the same. And this will be discussed in Sections III–V.

Since we only consider the transverse electric (TE) mode, i.e., both the transmitters and the receivers are infinitely long in the $\hat{y}$-direction and both the background medium and the inhomogeneous scatterers are invariant in the $\hat{y}$-direction, the scattered electric field at a receiver point $\boldsymbol{\rho}_r = \hat{x}x_r + \hat{z}z_r$ only has the $\hat{y}$-component and is evaluated by

$$E_y^{\text{sct}}(\boldsymbol{\rho}_r) = j\omega\varepsilon_0\epsilon_b \int_D G_{EJ}^{ri}(\boldsymbol{\rho}_r, \boldsymbol{\rho})\chi(\boldsymbol{\rho})E_y^{\text{tot}}(\boldsymbol{\rho})d\boldsymbol{\rho} \tag{1}$$

where

$$\chi(\boldsymbol{\rho}) = \frac{\epsilon_s(\boldsymbol{\rho}) - \epsilon_b}{\epsilon_b} \tag{2}$$

is the contrast of the 2-D scatterer with respect to the background medium, G_{EJ}^{ri} is the 2-D TE-mode layered medium

Green's function linking a field point $\boldsymbol{\rho} = \hat{x}x + \hat{z}z$ inside the inversion domain D and the receiver point $\boldsymbol{\rho}_r$, and E_y^{tot} is the total electric field inside D when the inhomogeneous 2-D scatterer is present. Note that (1) can be linearized based on Born approximation as long as the contrast is low. Therefore, for weak EM scattering scenarios, we have

$$E_y^{\text{sct}}(\boldsymbol{\rho}_r) = j\omega\varepsilon_0\epsilon_b \int_D G_{EJ}^{ri}(\boldsymbol{\rho}_r, \boldsymbol{\rho})\chi(\boldsymbol{\rho})E_y^{\text{inc}}(\boldsymbol{\rho})d\boldsymbol{\rho} \tag{3}$$

where E_y^{inc} is the incident electric field inside the inversion domain D when the 2-D scatterer is absent and it is evaluated by

$$E_y^{\text{inc}}(\boldsymbol{\rho}) = G_{EJ}^{it}(\boldsymbol{\rho}, \boldsymbol{\rho}_s)J_y(\boldsymbol{\rho}_s) \tag{4}$$

in which G_{EJ}^{it} is the 2-D TE-mode layered medium Green's function linking the source point $\boldsymbol{\rho}_s = \hat{x}x_s + \hat{z}z_s$ and the field point $\boldsymbol{\rho}$ inside D and J_y is the current density of the infinitesimal dipole transmitter at $\boldsymbol{\rho}_s$. According to the transmission line analogy method presented in [30], the 2-D TE-mode layered medium Green's functions can be computed by the 1-D inverse Fourier transforms

$$G_{EJ}^{ri}(\boldsymbol{\rho}_r, \boldsymbol{\rho}) = \frac{1}{2\pi}\int_{-\infty}^{+\infty} -V_i^h(k_x, z_r, z)e^{-jk_x(x_r - x)}dk_x \tag{5a}$$

$$G_{EJ}^{it}(\boldsymbol{\rho}, \boldsymbol{\rho}_s) = \frac{1}{2\pi}\int_{-\infty}^{+\infty} -V_i^h(k_x', z, z_s)e^{-jk_x'(x - x_s)}dk_x' \tag{5b}$$

where V_i^h is the spectral-domain voltage whose specific expression can be seen in Appendix A. Note that the superscript h stands for the TE mode and k_x and k_x' denote the wavenumbers in the horizontal direction. The superscript apostrophe means the EM wave is emitted from the source point at (x_s, z_s). By substituting (5b) into (4), (5a) into (3), and (4) into (3), we can obtain

$$\begin{aligned} &E_y^{\text{sct}}(\boldsymbol{\rho}_r) \\ &= \frac{j\omega\epsilon_b\varepsilon_0}{4\pi^2}\int_D\int_{-\infty}^{+\infty}\int_{-\infty}^{+\infty} V_i^h(k_x, z_r, z)V_i^h(k_x', z, z_s) \\ &\quad \cdot e^{-jk_x'(x - x_s)}e^{-jk_x(x_r - x)}dk_x'dk_x \cdot J_y(\boldsymbol{\rho}_s)\chi(\boldsymbol{\rho})d\boldsymbol{\rho} \\ &= \frac{j\omega\epsilon_b\varepsilon_0}{4\pi^2}\int_D\int_{-\infty}^{+\infty}\int_{-\infty}^{+\infty} V_i^h(k_x, z_r, z)V_i^h(k_x', z, z_s)\cdot J_y(\boldsymbol{\rho}_s) \\ &\quad \cdot e^{-j(k_x' - k_x)x}\cdot e^{jk_x'x_s}\cdot e^{-jk_xx_r}dk_x'dk_x\chi(x, z)dxdz \end{aligned} \tag{6}$$

where the detailed expression of $V_i^h(k_x, z_r, z)V_i^h(k_x', z, z_s)\cdot J_y(\boldsymbol{\rho}_s)$ can be seen in Appendix B. Then, we make following definitions:

$$\begin{cases} \eta = k_x' - k_x \\ \zeta_1 = k_{zm}' - k_{zm} \\ \zeta_2 = k_{zm}' + k_{zm} \\ \zeta_3 = -(k_{zm}' - k_{zm}) \\ \zeta_4 = -(k_{zm}' + k_{zm}) \end{cases} \tag{7a}$$

$$\begin{aligned} \widehat{\chi}_2^{(1)}(\eta, \zeta_1) &= \widehat{\chi}_4^{(1)}(\eta, \zeta_1) = \widehat{\chi}_1^{(2)}(\eta, \zeta_1) = \widehat{\chi}_2^{(2)}(\eta, \zeta_1) \\ &= \widehat{\chi}_4^{(2)}(\eta, \zeta_1) = \int_D \chi(x, z)e^{-j\eta x}e^{-j\zeta_1 z}dxdz \end{aligned} \tag{7b}$$

$$\begin{aligned} \widehat{\chi}_1^{(1)}(\eta, \zeta_2) &= \widehat{\chi}_3^{(1)}(\eta, \zeta_2) = \widehat{\chi}_5^{(1)}(\eta, \zeta_2) = \widehat{\chi}_3^{(2)}(\eta, \zeta_2) \\ &= \widehat{\chi}_5^{(2)}(\eta, \zeta_2) = \int_D \chi(x, z)e^{-j\eta x}e^{-j\zeta_2 z}dxdz \end{aligned} \tag{7c}$$

$$\begin{aligned} \widehat{\chi}_6^{(1)}(\eta, \zeta_3) &= \widehat{\chi}_8^{(1)}(\eta, \zeta_3) = \widehat{\chi}_{10}^{(1)}(\eta, \zeta_3) = \widehat{\chi}_8^{(2)}(\eta, \zeta_3) \\ &= \widehat{\chi}_{10}^{(2)}(\eta, \zeta_3) = \int_D \chi(x, z)e^{-j\eta x}e^{-j\zeta_3 z}dxdz \end{aligned} \tag{7d}$$

$$\begin{aligned} \widehat{\chi}_7^{(1)}(\eta, \zeta_4) &= \widehat{\chi}_9^{(1)}(\eta, \zeta_4) = \widehat{\chi}_6^{(2)}(\eta, \zeta_4) = \widehat{\chi}_7^{(2)}(\eta, \zeta_4) \\ &= \widehat{\chi}_9^{(2)}(\eta, \zeta_4) = \int_D \chi(x, z)e^{-j\eta x}e^{-j\zeta_4 z}dxdz \end{aligned} \tag{7e}$$

and thus (6) can be rewritten as

$$\begin{aligned} &E_y^{\text{sct}}(\boldsymbol{\rho}_r) \\ &= \frac{j\omega\epsilon_b\varepsilon_0}{4\pi^2}\int_{-\infty}^{+\infty}\int_{-\infty}^{+\infty}\sum_{n=1}^{10} f_n\cdot\widehat{\chi}_n\cdot e^{jk_x'x_s}\cdot e^{-jk_xx_r}dk_x'dk_x \end{aligned} \tag{8}$$

where f_n can take $f_n^{(1)}$ or $f_n^{(2)}$ and $\widehat{\chi}_n$ is the contrast spatial spectrum which can take $\widehat{\chi}_n^{(1)}$ or $\widehat{\chi}_n^{(2)}$. The superscript "(1)" means the transmitter array and the receiver array are located on the same side of the inversion domain D while the superscript "(2)" means they are located on two sides. Note that f_n is actually the coefficient connecting $\widehat{\chi}_n$ and the scattered field spectrum at the receiver array. Its detailed expression can be seen in Appendix B. One should note that, from a physical point of view, the four $\hat{z}$-direction spectral variables ζ_1, ζ_2, ζ_3, and ζ_4 in (7a) correspond to four different EM wave propagation pictures at a certain field point (x, z) inside the inversion domain. The variable ζ_1 depicts the incident wave arriving at the field point in the $+\hat{z}$-direction and the scattered wave escaping away from it also in the $+\hat{z}$-direction. In contrast, the variable ζ_2 depicts the incident wave arriving at the field point in the $+\hat{z}$-direction but the scattered wave escaping away from it in the $-\hat{z}$-direction. The variables ζ_3 and ζ_4 depict the wave propagation pictures which are completely opposite to those depicted by ζ_1 and ζ_2, respectively. Obviously, only ζ_2 exists for a two-layer model as discussed in the previous work [25] since the EM wave reflection and transmission in multiple layer boundaries vanish.

Finally, we assume that the transmitter continuously varies its position in the $z = z_s$ horizontal line and the receiver also continuously varies its position in the $z = z_r$ horizontal line and define the spectrum of the scattered electric field at the receiver array as

$$\begin{aligned} &\widetilde{E_y}^{\text{sct}}(k_x, k_x') \\ &= \int_{-\infty}^{+\infty}\int_{-\infty}^{+\infty} E_y^{\text{sct}}(x_s, x_r)e^{-jk_x'x_s + jk_xx_r}dx_sdx_r \end{aligned} \tag{9}$$

and thus (8) can be expressed in a compact form

$$\widetilde{E_y}^{\text{sct}} = j\omega\epsilon_b\varepsilon_0\cdot\sum_{n=1}^{10} f_n\cdot\widehat{\chi}_n \tag{10}$$

in which the summation is caused by reflection and transmission in multiple planar boundaries. In other words, the reconstructable spectrum of the 2-D contrast not only depends on the scattered EM waves directly propagating from the scatterer to the receiver array but is also contributed by

the waves generated from multiple boundary reflections and transmissions. In addition, the coefficient f_n which is also closely related to boundary reflections actually weights the reconstructable spectrum.

III. Influence of Transceiver Array Aperture Size on 2-D FWI in Multilayered Media: Theoretical Analysis

In this section, we give a theoretical analysis of how the transceiver array aperture size influences the inversion of 2-D scatterers embedded in a planarly multilayered medium. Specifically speaking, we evaluate the quantitative relationship between the transceiver array aperture size and the spectrum bandwidth of the reconstructable contrast χ not only for four individual wave propagation pictures at the field point (x, z) as described by ζ_1, ζ_2, ζ_3, and ζ_4 in (7a) but also for the overall picture as described by the summation given in (10). For convenience to perform theoretical analysis, we suppose that the whole background space is lossless and is divided into five layers by the horizontal interfaces located at $z_1 = -0.8$ m, $z_2 = 0.0$ m, $z_3 = 3.16$ m, and $z_4 = 3.66$ m, respectively. The relative permittivity parameters in five layers are $\varepsilon_b^1 = 1.5$, $\varepsilon_b^2 = 1.0$, $\varepsilon_b^3 = 9.0$, $\varepsilon_b^4 = 1.0$, and $\varepsilon_b^5 = 2.0$, respectively. The 2-D scatterers are located inside the third layer (i.e., $m = 3$) with $\sigma_s(x, z) = 0$. The operation frequency is 300 MHz. Other parameters related to the inversion domain D are $a = 0.75$ m, $c = 0.92$ m, and $z_{\min} = 0.66$ m. The transmitter array and the receiver array can be located on the same side of the inversion domain D with $z_s = z_r = z_2$ or on two different sides with $z_s = z_2$ and $z_r = z_3$. Note that the transceiver arrays are assumed to coincide with layer interfaces in this work. Meanwhile, it is also assumed that the inversion domain D is far enough from two adjacent horizontal interfaces at $z = z_2$ and $z = z_3$, and thus the effect of the evanescent wave on the computation of the theoretically reconstructable spectrum of the 2-D scatterer placed between them is neglected. Here, "theoretically" means the computed reconstructable spectrum is only determined by the valid wavenumber ranges and the effects of evanescent mode, noise contamination, subsurface signal attenuation, and so on are neglected.

Therefore, let us now correlate the transceiver array aperture sizes with the valid wavenumber ranges and quantitatively analyze their effects on the reconstructable spectrum of the 2-D scatterer embedded inside a planarly multilayered medium. We take the same approximation suggested in [25, Section III] and assume the dominant energy of the EM wave propagating between a fictitious equivalent source point inside the domain D and a receiver point or a transmitter point like a plane wave. Reducing the transceiver array aperture size, i.e., decreasing x_M, is equivalent to decreasing the array angle θ_x defined in Fig. 2. Therefore, obeying the plane wave assumption mentioned above, the valid wavenumbers automatically satisfy

$$|k_x'|, |k_x| < k_b \sin\theta_x = \frac{k_b |x_M + a|}{\sqrt{(x_M + a)^2 + (2c + z_s + z_{\min})^2}} \tag{11a}$$

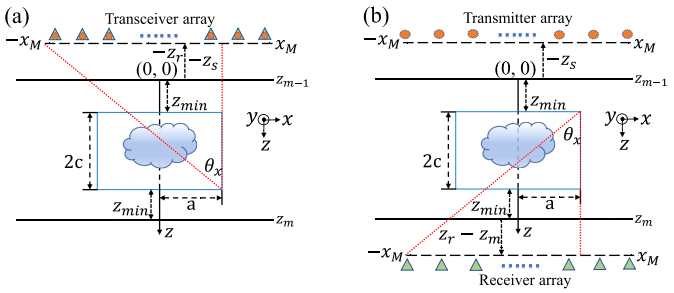

Fig. 2. Definition of the array angle used to denote the array aperture size. (a) θ_x for the transmitter array and the receiver array when they are located on the same side of the inversion domain D. (b) θ_x for the receiver array when it is located on the opposite side of the transmitter array.

$$|k_x| < k_b \sin\theta_x = \frac{k_b |x_M + a|}{\sqrt{(x_M + a)^2 + (z_r - z_{\min})^2}} \tag{11b}$$

where k_b is the wavenumber of the background layer in which the inversion domain is located. Equation (11a) gives the valid ranges of the wavenumbers for the incident wave and the scattered wave when the transmitter array and the receiver array are located on the same side of the inversion domain D with $z_s = z_r$. However, as shown in Fig. 2(b), when the receiver array is placed on the opposite side of the domain D, the valid range of the scattered wavenumber is given in (11b). Because we set $z_s = z_r = z_{m-1}$ when the transmitter array and the receiver array are located on the same side and $z_s = z_{m-1}$ and $z_r = z_m$ when they are located on different sides of the inversion domain D, the incident EM wave and the scattered wave share the same angle θ_x. Consequently, k_x' and k_x vary in the same range. We now let them be subject to the inequality in (11) in accordance with the transceiver array aperture size limitation to guarantee both the incident and the scattered waves can normally propagate and obtain the 2-D reconstructable spectrum of the scatterer contrast.

In order to vividly show how the reconstructable 2-D spectrum varies with the transceiver array aperture size, we let x_M take four representative values $+\infty$, 3.5, 1.75, and 0.75 m. The corresponding four values of θ_x are 90°, 60°, 45°, and 30°, respectively. Fig. 3 shows the four theoretically reconstructable spectral components of the 2-D scatterer contrasts for different θ_x values. Three observations are made here. First, since the incident EM wave can arrive at the inversion domain D in either the $+\hat{z}$-direction or the $-\hat{z}$-direction and the scattered wave can escape away from it also in either the $+\hat{z}$-direction or the $-\hat{z}$-direction, the computed reconstructable spectra have four different components, which are different from that shown in [25, Fig. 2]. The $\eta\zeta_1$ and $\eta\zeta_3$ spectral components shown in Fig. 3(a) and (c) actually display the theoretically reconstructable spectra of the contrast of the 2-D scatterer when the EM wave impinges upon it and leaves from it in the same $\hat{z}$-direction. In contrast, the $\eta\zeta_2$ and $\eta\zeta_4$ spectral components shown in Fig. 3(b) and (d) display the spectra when the EM wave impinges upon the scatterer and leaves from it in the opposite $\hat{z}$-directions. The positive and negative spatial frequency variables for η and ζ are actually caused by different combinations of incident wave directions and scattered wave directions. For example, Fig. 3(b) and (d) actually shows

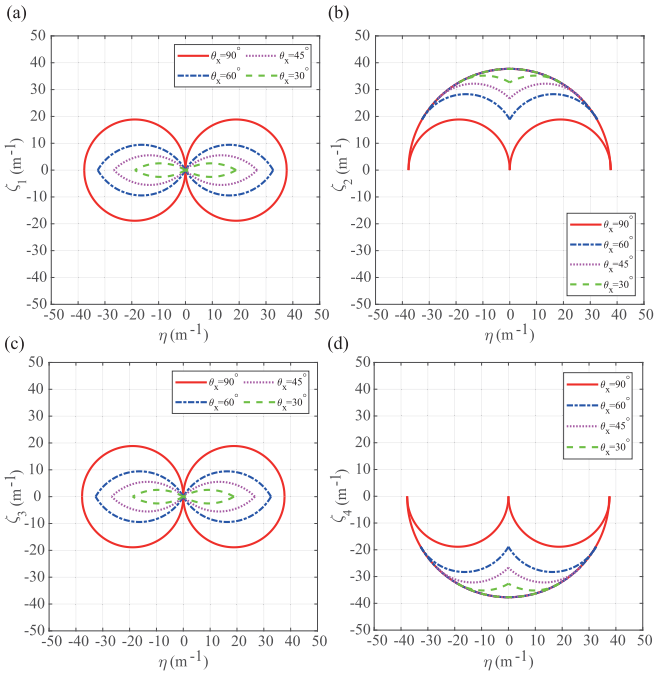

Fig. 3. Different theoretically reconstructable spectral components of the contrast of the 2-D scatterer embedded inside a multilayered medium when the transceiver arrays have different aperture sizes. (a) $\eta\zeta_1$ spectral components. (b) $\eta\zeta_2$ spectral components. (c) $\eta\zeta_3$ spectral components. (d) $\eta\zeta_4$ spectral components. Each theoretical 2-D spectrum is enclosed within a closed curve.

the same reconstructable 2-D spectrum although the spatial frequency variable ζ has opposite values. Such a phenomenon is not observed for a half-space model, as shown in [25, Fig. 2]. When the multiple reflections from multiple layer boundaries disappear, the incident wave can only arrive at the scatterer in a single $\hat{z}$-direction and the scattered wave also leaves from it in a single $\hat{z}$-direction. As a result, only the $\eta\zeta_2$ spectral component remains. Second, for the $\eta\zeta_1$ and $\eta\zeta_3$ spectral components shown in Fig. 3(a) and (c), the major spectral contents in the vertical $\hat{\zeta}$-direction concentrate in the low-frequency band. However, most spectral contents in the vertical $\hat{\zeta}$-direction concentrate in the high-frequency band for the $\eta\zeta_2$ and $\eta\zeta_4$ spectral components, as shown in Fig. 3(b) and (d). Such a discrepancy is as we expect. From a mathematical point of view, ζ_1 and ζ_3 are equivalent to the difference of k_z' and k_z of the background layer while ζ_2 and ζ_4 are equivalent to the summation of k_z' and k_z. Therefore, the low-frequency content shows up in the $\eta\zeta_1$ and $\eta\zeta_3$ spectra due to the wavenumber cancellation while high-frequency content shows up in the $\eta\zeta_2$ and $\eta\zeta_4$ spectra due to the wavenumber superposition. From a physical point of view, if the incident EM wave arrives at the scatterer and leaves from it in the same direction, the observable spectrum of the scatterer is squeezed due to the spatial frequency cancellation. In the extreme case, when the incident wave and the scattered wave have the exactly same spatial frequency, no spatial fluctuation of the inversion domain is observed by the EM waves and thus only the zero frequency content is obtained. In contrast, if the incident EM wave arrives at the scatterer and leaves from it in the opposite directions, the scatterer contrast must exist inside the background layer to reflect the incident wave. As a result, the high-frequency content of the scatterer is directly observed. Third, when the transceiver array aperture size gradually decreases from $\theta_x = 90°$ to $\theta_x = 30°$, all four components of the 2-D reconstructable spectrum show the "lowpass" feature in the horizontal $\hat{x}$-direction with the cutoff spatial frequency of $2k_b$ which is determined by the EM wave frequency, as shown in Fig. 3. However, in the vertical $\hat{z}$-direction, the $\eta\zeta_1$ and $\eta\zeta_3$ spectral components also show the "lowpass" feature but the $\eta\zeta_2$ and $\eta\zeta_4$ spectral components show the "bandpass" feature with the upper limit cutoff spatial frequency of $2k_b$. From a mathematical point of view, according to (11), decreasing θ_x value actually narrows down the variation ranges of k_x' and k_x close to the zero frequency but narrows down the variation ranges of k_z' and k_z close to k_b. Because k_x' and k_x are canceled with each other in the horizontal $\hat{x}$-direction for all four spectral components and k_z' and k_z are canceled with each other in the vertical $\hat{z}$-direction for the $\eta\zeta_1$ and $\eta\zeta_3$ spectral components, narrowing down their variation ranges will naturally force the reconstructable 2-D spectrum to converge to the zero spatial frequency and thus a "lowpass" phenomenon is observed. In contrast, because k_z' and k_z are superposed with each other in the vertical $\hat{z}$-direction for the $\eta\zeta_2$ and $\eta\zeta_4$ spectral components, narrowing down their variation ranges close to k_b will naturally force the reconstructable 2-D spectrum to converge to the frequency of $2k_b$ and thus a "bandpass" phenomenon is observed. From a physical point of view, decreasing the transceiver array aperture size is equivalent to retaining the energy of both the incident wave and the scattered wave in the vertical $\hat{z}$-direction but reducing their energy in the horizontal $\hat{x}$-direction, which automatically deteriorates the horizontal resolution of the reconstruction. Meanwhile, the maximum $\hat{\zeta}$-direction spatial frequency of the reconstructable 2-D spectrum remains unchanged no matter how the array aperture size is changed since the scatterer can always be illuminated by the vertical incident and reflected waves.

Fig. 4 shows the overall reconstructable spectra of the 2-D scatterer for different transceiver array aperture sizes. An overall spectrum is the superposition of four components shown in Fig. 3 and different colors represent the contributions from different components. Two points must be emphasized here. First, when θ_x becomes 90°, i.e., the array aperture size is infinitely large, the theoretically reconstructable spectrum becomes an ideal circular disk with the radius of $2k_b$, as shown in Fig. 4(a). An infinitely large array aperture size means the 2-D scatterer can be illuminated by the EM waves from 360° and the scattered waves also leave from the scatterer in 360°. Therefore, the observable spectrum reaches the maximum value $2k_b$ in 360°. Second, reducing the transceiver array aperture size leads to the "bandstop" feature of the reconstructable spectrum in the vertical $\hat{z}$-direction. When the incident and scattered wave vectors gradually approach the vertical $\hat{z}$-direction, the reflected wave from the scatterer detects its spatially high-frequency variations while the transmitted wave passing through the scatterer detects its spatially low-frequency variations, which leads to the "bandstop" feature in the vertical $\hat{z}$-direction.

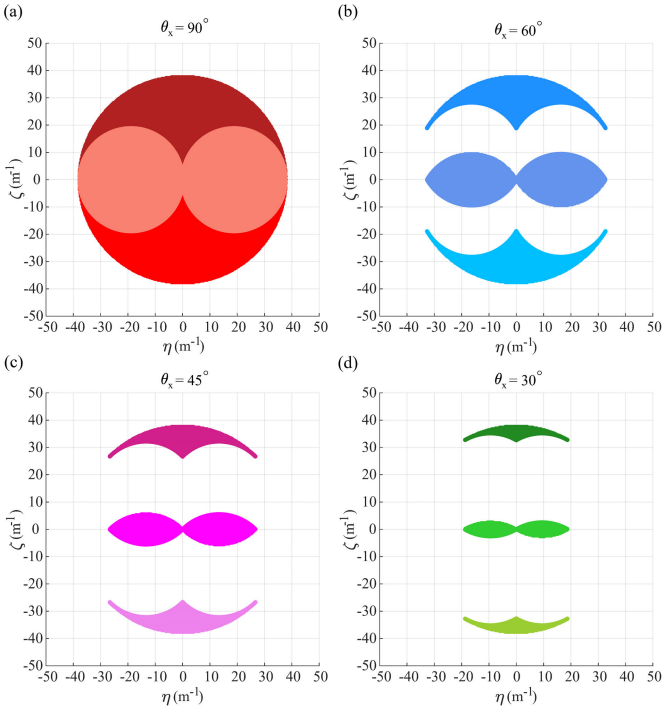

Fig. 4. Overall theoretically reconstructable spectrum of the 2-D scatterer embedded inside a multilayered medium when the transceiver array has the aperture size with (a) $\theta_x = 90°$, (b) $\theta_x = 60°$, (c) $\theta_x = 45°$, and (d) $\theta_x = 30°$.

IV. Influence of Transceiver Array Aperture Size on 2-D FWI in Multilayered Media: SVD Analysis

In this section, we will focus on more practical 2-D EM inverse scattering scenarios in the circumstance of multilayered media. Specifically speaking, we will keep investigating how the transceiver array aperture size influences the reconstruction of 2-D scatterers embedded inside a multilayered medium but with the effects of wave attenuation and evanescent mode taken into account. As a result, the relationship between the spectrum of the scattered EM field recorded at the receiver array and the reconstructable spectrum of the 2-D scatterers described in (10) is no longer precise. Therefore, the SVD method proposed in [25, Section IV] is adopted to search for the solution of χ for the EM inverse scattering problem described in (6).

We first define the linear integral operator $\mathcal{I}$ mapping the contrast χ distribution inside the 2-D inversion domain D to the scalar scattered electric field data recorded at the receiver array

$$\mathcal{I} : \chi \in \mathcal{M} \to E_y^{\mathrm{sct}} \in \mathcal{D} \tag{12}$$

where $\mathcal{M}$ is the model space within which the best solution of χ is searched for and $\mathcal{D}$ is the data space in which the scalar scattered electric field data distributes. In addition, both $\mathcal{M}$ and $\mathcal{D}$ can be treated as Hilbert spaces and thus the L^2 inner products denoted by $\langle \cdot, \cdot \rangle_{\mathcal{M}}$ and $\langle \cdot, \cdot \rangle_{\mathcal{D}}$ can be defined for them, respectively [25]. Meanwhile, the SVD operation is allowed to apply to $\mathcal{I}$ since it acts on $\mathcal{M}$ and $\mathcal{D}$ continuously and can be treated as a compact operator [31]. Therefore, we define the singular system $\{\Sigma_n, \mathbf{U}_n, \mathbf{V}_n\}_{n=1}^{\infty}$ of the operator $\mathcal{I}$ where Σ_n is the nth singular value, $\mathbf{U}_n$ is the nth left-singular function, and $\mathbf{V}_n$ is the nth right-singular function. Therefore, the reconstructed contrast χ in (6) can be written as [31]

$$\chi = \sum_{n=1}^{\infty} \frac{1}{\Sigma_n} < \mathbf{E}_y^{\mathrm{sct}},\ \mathbf{U}_n >_D \mathbf{V}_n \tag{13}$$

where Σ_n is ordered in descending with the increase of n, $\boldsymbol{\chi}$ is a column vector containing all the contrast values in the 2-D inversion domain, and $\mathbf{E}_y^{\mathrm{sct}}$ is a column vector containing the scalar scattered electric field values sampled in all the receiver points. One should note that the major performance of the operator $\mathcal{I}$ is determined by its large singular values and small ones easily lead to the solution instability due to the numerical error in the computation. Therefore, the truncated SVD expansion is used to suppress the amplification of the scattered field data error and thus approximate the stable contrast solution of the 2-D scatterer [32]

$$\chi \approx \sum_{n=1}^{N} \frac{1}{\Sigma_n} < \mathbf{E}_y^{\mathrm{sct}},\ \mathbf{U}_n >_D \mathbf{V}_n \tag{14}$$

where N is the threshold for singular values and determined by a hypothetical signal noise ratio (SNR). We then discretize the inversion domain D into $P \times Q$ rectangular pixels and numerically perform the SVD since the operator $\mathcal{I}$ is continuous. Meanwhile, we expand the contrast function χ by 1-D piecewise constant functions in both the $\hat{x}$-direction and $\hat{z}$-direction

$$\chi(x, z) = \sum_{p,q} \chi_{pq} \cdot \Pi(x - x_p; \Delta x) \cdot \Pi(z - z_q; \Delta z) \tag{15}$$

where $\Delta x = (2a/P)$ and $\Delta z = (2c/Q)$ are the supports of the 1-D piecewise constant functions in the $\hat{x}$- and $\hat{z}$- directions, respectively, and χ_{pq} is the expansion coefficient. By substituting (15) into (6) and separately executing $\int_D \{\cdot\} dx$ and $\int_D \{\cdot\} dz$ with respect to χ based on the expression of V_i^h given in Appendix A, we obtain

$$\hat{\phi}_p = 2\frac{\sin\left[(k_x' - k_x)\left(\frac{\Delta x}{2}\right)\right]}{k_x' - k_x} e^{-j(k_x' - k_x)x_p} \tag{16a}$$

$$\hat{\psi}_{q,2}^{(1)} = \hat{\psi}_{q,4}^{(1)} = \hat{\psi}_{q,1}^{(2)} = \hat{\psi}_{q,2}^{(2)} = \hat{\psi}_{q,4}^{(2)} = 2\frac{\sin\left[(k_{zm}' - k_{zm})\left(\frac{\Delta z}{2}\right)\right]}{k_{zm}' - k_{zm}} e^{-j(k_{zm}' - k_{zm})z_q} \tag{16b}$$

$$\hat{\psi}_{q,1}^{(1)} = \hat{\psi}_{q,3}^{(1)} = \hat{\psi}_{q,5}^{(1)} = \hat{\psi}_{q,3}^{(2)} = \hat{\psi}_{q,5}^{(2)} = 2\frac{\sin\left[(k_{zm}' + k_{zm})\left(\frac{\Delta z}{2}\right)\right]}{k_{zm}' + k_{zm}} e^{-j(k_{zm}' + k_{zm})z_q} \tag{16c}$$

$$\hat{\psi}_{q,6}^{(1)} = \hat{\psi}_{q,8}^{(1)} = \hat{\psi}_{q,10}^{(1)} = \hat{\psi}_{q,8}^{(2)} = \hat{\psi}_{q,10}^{(2)} = 2\frac{\sin\left[(k_{zm}' - k_{zm})\left(\frac{\Delta z}{2}\right)\right]}{k_{zm}' - k_{zm}} e^{j(k_{zm}' - k_{zm})z_q} \tag{16d}$$

$$\hat{\psi}_{q,7}^{(1)} = \hat{\psi}_{q,9}^{(1)} = \hat{\psi}_{q,6}^{(2)} = \hat{\psi}_{q,7}^{(2)} = \hat{\psi}_{q,9}^{(2)} = 2\frac{\sin\left[(k_{zm}' + k_{zm})\left(\frac{\Delta z}{2}\right)\right]}{k_{zm}' + k_{zm}} e^{j(k_{zm}' + k_{zm})z_q} \tag{16e}$$

where x_p and z_q are the central coordinates of the 1-D constant functions. The superscript and subscript of $\hat{\psi}_q$ indicate the relative positions of the transmitter array and the receiver array and which spectral component is invoked, respectively. For

example, $\hat{\psi}_{q,8}^{(2)}$ means the transmitter array and the receiver array are located on two sides of the inversion domain D and the $\eta\zeta_3$ spectral component corresponding to $\widehat{\chi}_8^{(2)}$ in (7d) is invoked. Finally, by substituting (16) into (6), we obtain the approximation

$$E_y^{\text{sct}}(\boldsymbol{\rho}_r, \boldsymbol{\rho}_s) \approx \frac{j\omega\epsilon_b\varepsilon_0}{4\pi^2} \sum_{p,q} \chi_{pq} \int\!\!\int_{-\infty}^{+\infty} \hat{\phi}_p(k_x', k_x) \cdot \sum_{n=1}^{10} \left[f_n(k_x', k_x) \cdot \hat{\psi}_{q,n}(k_x', k_x) \right] \cdot e^{-j(k_x x_r - k_x' x_s)} dk_x' dk_x \quad (17)$$

in which $\hat{\psi}_{q,n}$ can take $\hat{\psi}_{q,n}^{(1)}$ or $\hat{\psi}_{q,n}^{(2)}$ and the EM wave reflections and transmissions in multiple layer interfaces are completely reflected in f_n. By sampling the scattered electric fields in a series of discrete points x_r at the $z = z_r$ horizontal line when the excitation line sources are also located in a series of discrete points x_s at the $z = z_s$ line, we can rewrite (17) in a compact form

$$\mathbf{E}_y^{\text{sct}} = \mathbf{A}\boldsymbol{\chi} \quad (18)$$

where $\mathbf{A}$ with the dimensions of $N_{tx}N_{rx} \times PQ$ is actually the discrete matrix form of the integral operator $\mathcal{I}$. Here, N_{tx} and N_{rx} respectively represent the transmitter and receiver numbers in the horizontal $\hat{x}$-direction. Note that we let them be exactly the same in this work to guarantee the transmitter array and the receiver array are completely overlapped or placed symmetrically to the inversion domain D. In addition, the interval between two adjacent discrete points x_r at the $z = z_r$ horizontal line and that between two adjacent discrete points x_s at the $z = z_s$ horizontal line are 0.25 m. This spatial sampling density of four points per wavelength is able to guarantee computation accuracy according to the Nyquist sampling theorem.

Now, let us still choose the four representative transceiver array aperture sizes adopted in Section III but replace $\theta_x = 90°$ with $\theta_x = 88°$ to avoid the difficulty in implementing numerical simulation, and apply SVD to the corresponding $\mathbf{A}$ matrices to compute the singular value distributions and the right-singular functions. Meanwhile, we assume the planarly layered background medium has the conductivity values $\sigma_b^1 = 0.002$ S/m, $\sigma_b^3 = 0.001$ S/m, and $\sigma_b^5 = 0.003$ S/m to account for the wave attenuation. Other model parameters and the operation frequency are the same as those mentioned in Section III. Because the reconstructed contrast distribution is manifested by the right-singular functions based on (14), we apply the Fourier transforms to the first N right-singular vectors and their summation actually represents the 2-D spectrum of the contrast. Therefore, we define the spectrum

$$sp(\eta, \zeta) = \sum_{n=1}^{N} \left| \widetilde{\mathbf{V}}_n(\eta, \zeta) \right| \quad (19)$$

where

$$\widetilde{\mathbf{V}}_n(\eta, \zeta) = \int_D \mathbf{V}_n(x, z) \exp[-j(\eta x + \zeta z)] dx dz = \sum_{p,q} \mathbf{V}_n(x_p, z_q) \exp[-j(\eta x_p + \zeta z_q)] \Delta S \quad (20)$$

in which ΔS is the area of each discrete pixel in the inversion domain and the ranges of η and ζ are set as $-50 \le \eta, \zeta \le 50$. Note that this range for η and ζ is large enough to incorporate all the spectral contents obtained from both theoretical analysis and SVD analysis according to (7a) and (11) as well as the background dielectric parameters and operation frequency. In addition, in order to guarantee the stability of the computed spectrum, N in (19) is set according to -20 dB SNR, i.e., the minimum singular value used in the computation is greater than 10% of the largest singular value Σ_1. The obtained normalized singular value variations and spectra of right-singular functions for different array aperture sizes and different spectral components when the transmitter array and the receiver array are located on the same side and on two sides of the inversion domain are shown in Figs. 5 and 6, respectively. Four observations are made here. First, the computed spectra of the right-singular functions are roughly consistent with the theoretically reconstructable ones for all four components no matter whether the transmitter and receiver arrays are located on the same side or different sides of the inversion domain. All spectra show the "lowpass" feature in the horizontal $\hat{x}$-direction but the "bandpass" feature in the vertical $\hat{z}$-direction with the decrease in the transceiver array aperture size. The smaller is the array aperture size, the less singular values are observed for a certain SNR threshold. Second, the smaller is the array aperture size, the more spectral contents of the right-singular functions exceed the boundaries of the theoretically reconstructable spectra. This is because we have assumed that the major energy of the incident and scattered EM fields concentrates in the plane waves and the reflections in multiple layer boundaries are omitted when theoretically reconstructable spectra are evaluated. However, for the numerical computation of right-singular function spectra, the contributions from both 2-D line source Green's functions and multiple layer reflections are taken into account. As a result, the smaller is the array aperture size, the more extra spectral contents generated by the additional contribution from the cylindrical waves excited by line sources and multiple layer reflections are superposed to the theoretically reconstructable spectra. Third, although $\eta\zeta_1$ and $\eta\zeta_3$ spectral components concentrate in the low-frequency band and $\eta\zeta_2$ and $\eta\zeta_4$ spectral components concentrate in the high-frequency band, the $\eta\zeta_1$ and $\eta\zeta_3$ spectral components have more singular values than the $\eta\zeta_2$ and $\eta\zeta_4$ spectral components for a certain SNR threshold and thus the broader bandwidth, no matter whether the transmitter and receiver arrays are located on the same side or different sides of the inversion domain. The $\eta\zeta_1$ and $\eta\zeta_3$ spectral components correspond to the physics picture that the EM wave penetrates the scatterer while the $\eta\zeta_2$ and $\eta\zeta_4$ spectral components correspond to the physics picture that the EM wave is reflected by the scatterer. Therefore, the $\eta\zeta_1$ and $\eta\zeta_3$ spectral components naturally have broader bandwidth since the scatterer is more thoroughly illuminated by transmitting waves. Fourth, the $\eta\zeta_1$ and $\eta\zeta_3$ spectral components are exactly the same when the transmitter and receiver arrays are located on the same side of the inversion domain while the $\eta\zeta_2$ and $\eta\zeta_4$ spectral components are exactly symmetrical when the transmitter and receiver arrays are

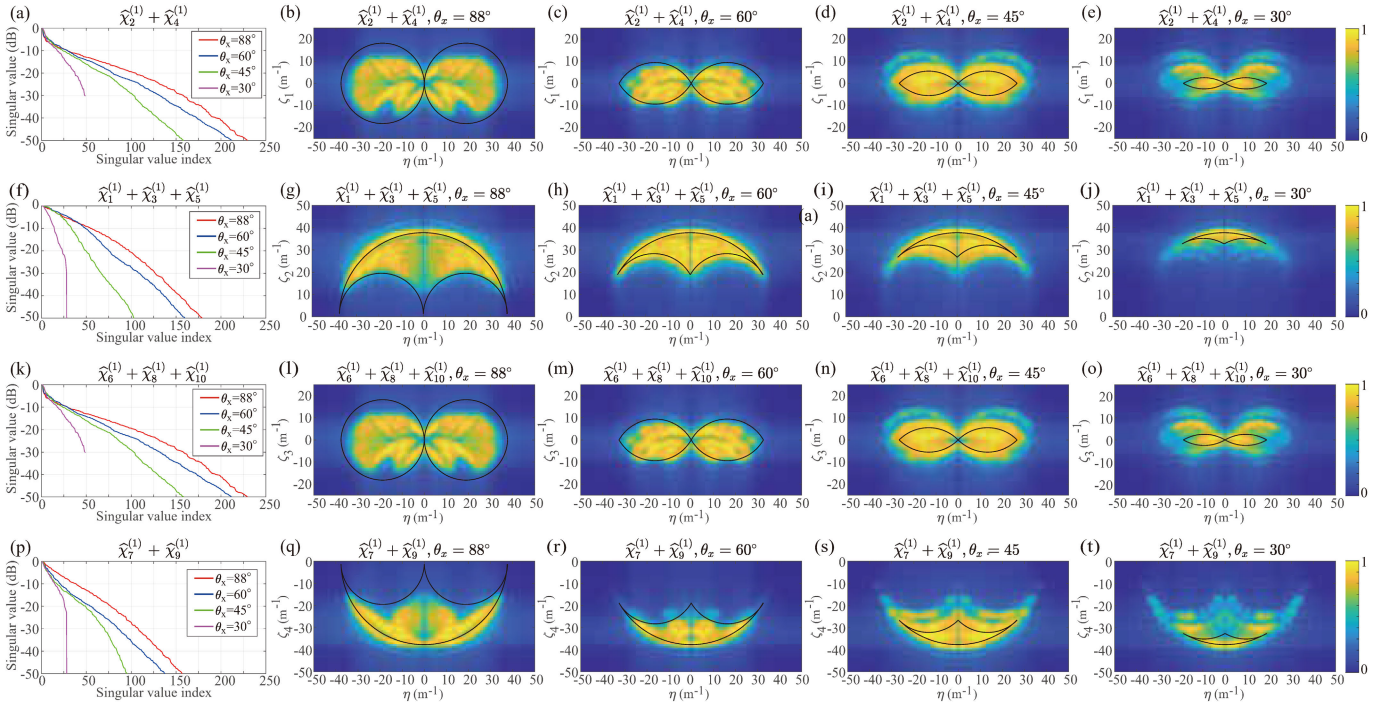

Fig. 5. Singular values of the discretized integral operator obtained by SVD and comparisons of the 2-D spectra of the corresponding right-singular functions and 2-D theoretically reconstructable contrast spectra for four representative aperture sizes when the transmitter array and the receiver array are located on the same side of the inversion domain. Different rows show different spectral components. The first column shows the singular values of different spectral components. Columns 2–5 show the 2-D spectra for different aperture sizes. Each theoretical 2-D spectrum is enclosed with a closed black curve.

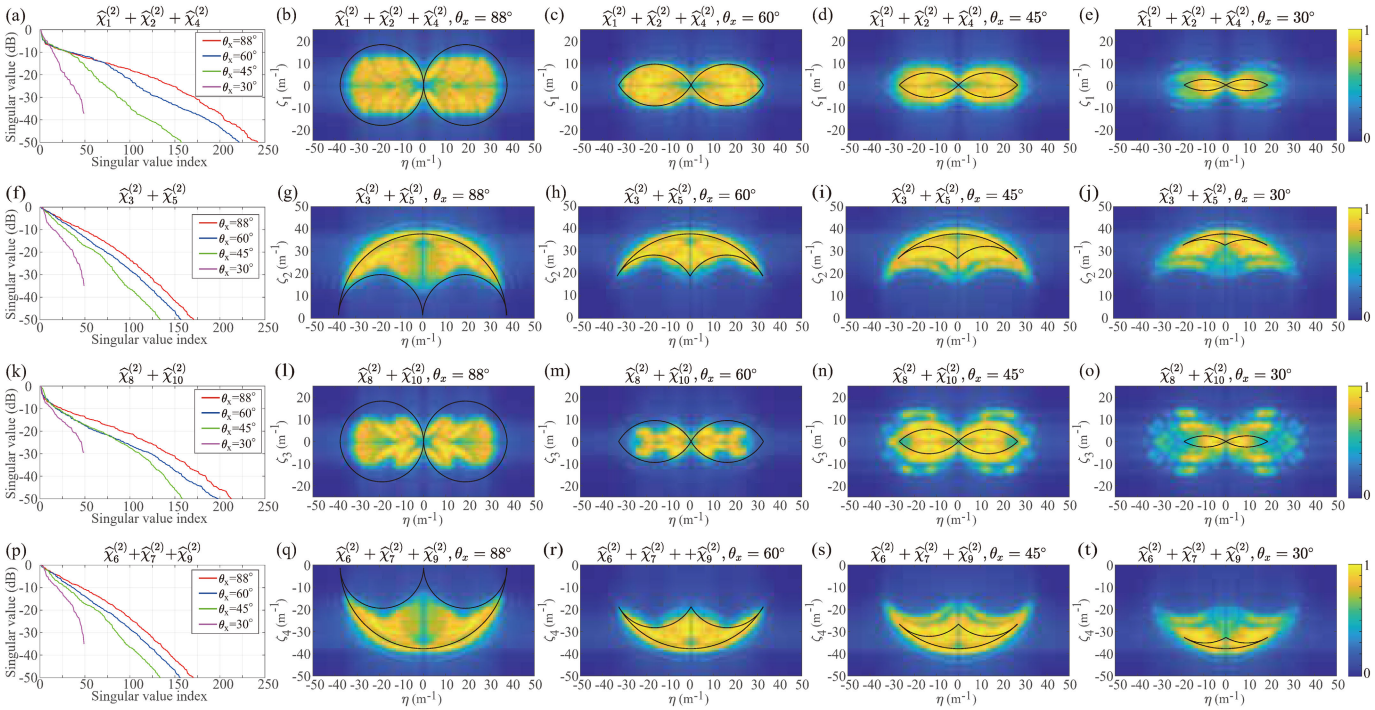

Fig. 6. Singular values of the discretized integral operator obtained by SVD and comparisons of the 2-D spectra of the corresponding right-singular functions and 2-D theoretically reconstructable contrast spectra for four representative aperture sizes when the transmitter array and the receiver array are located on two sides of the inversion domain. Different rows show different spectral components. The first column shows the singular values of different spectral components. Columns 2–5 show the 2-D spectra for different aperture sizes. Each theoretical 2-D spectrum is enclosed with a closed black curve.

located on two sides of the inversion domain. These high consistencies are caused by the exactly same wave propagation picture inside the inversion domain. In addition, either the $\eta\zeta_1$ or $\eta\zeta_3$ spectral component is exactly self-symmetrical with respect to $\zeta = 0$ when the transmitter and receiver arrays are located on two sides of the inversion domain. This is because the transmitter and receiver arrays are placed exactly symmetrical about the inversion domain.

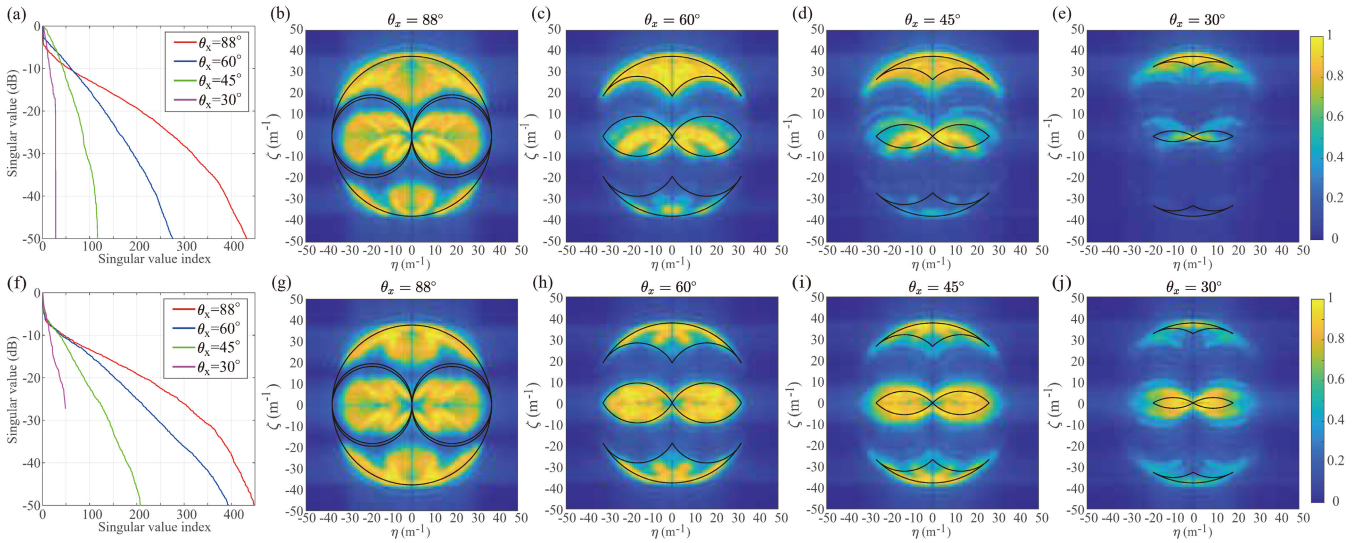

Fig. 7. Singular values of the discretized integral operator obtained by SVD and comparisons of the 2-D spectra of the corresponding right-singular functions and 2-D theoretically reconstructable contrast spectra for four representative aperture sizes when the transmitter array and the receiver array are located (a)–(e) on the same side of the inversion domain and (f)–(j) on two sides. The first column shows the singular values. Columns 2–5 show the overall 2-D spectra for different aperture sizes. Each overall theoretical 2-D spectrum is enclosed with closed black curves.

Fig. 7 shows comparisons of the overall spectra of the right-singular functions and the overall theoretical 2-D spectra as well as the corresponding singular value variations. As we expect, the overall spectra have the obvious "bandstop" feature in the vertical $\hat{z}$-direction, but still show the "lowpass" feature in the horizontal $\hat{x}$-direction. They have strong symmetry in the vertical direction when the transmitter array and the receiver array are placed on two sides of the inversion domain. In contrast, the spectral energy intensely concentrates in the upper half-space in the $\eta\zeta$ plane when the transmitter array and the receiver array are placed on the top side of the inversion domain. Such an asymmetry is as we expect. Because both the transmitter array and the receiver array are placed on the same side, the directly reflected EM wave from the scatterer of course will dominate in the inversion. The influence of the EM wave transmitting the scatterer and finally reflected back by another boundary will be weakened. Another interesting observation is that the overall reconstructable spectral bandwidth manifested via the right-singular functions for a small transceiver array aperture size when the transmitter and receiver arrays are placed on two sides of the inversion domain is wider than that when the transmitter and receiver arrays are placed on the same side. For a smaller array aperture size, the scatterer is illuminated more thoroughly if the transmitter and receiver arrays are placed on two sides and thus the reconstructable spectral bandwidth is wider. However, this superiority will be lost if the array aperture size becomes very large, e.g., $\theta_x = 88°$ since in this situation the scatterer still can be illuminated thoroughly from the left and right sides even when both the transmitter and the receiver arrays are placed on the top side.

V. Influence of Transceiver Array Aperture Size on 2-D FWI in Multilayered Media: Numerical Validation

In this section, the theoretical analysis results and the SVD analysis results presented in Sections III and IV are validated by several numerical experiments. We use the same inversion configurations adopted in Section III but place a series of rectangular scatterers inside the inversion domain, as shown in Fig. 8(a) and (f). All scatterers have the same dielectric parameters $\varepsilon_s = 9.2$ and $\sigma_s = 1.2$ mS/m. In addition, the spatial fluctuation from the left column to the right column for the scatterers becomes faster and faster. The scattered electric fields recorded at the receiver array are synthesized by the stabilized biconjugate-gradient fast Fourier transform (BCGS-FFT) solver [33]. The FWI is accomplished by the conjugate gradient solver based on the sensitivity matrix directly assembled by incident fields, i.e., based on Born approximation. Fig. 8(b)–(e) shows the reconstructed 2-D profiles of the contrast moduli for four representative aperture sizes when the transmitter array and the receiver array are located on the same side of the inversion domain while Fig. 8(g)–(j) shows the results when the transmitter array and the receiver array are located on two sides. Three observations are made. First, the "lowpass" phenomenon is obvious in the horizontal $\hat{x}$-direction. The smaller is the transceiver array aperture size, the more obscure are the boundaries of the reconstructed contrast profiles in the horizontal direction. Second, the "bandstop" phenomenon is obvious in the vertical $\hat{z}$-direction. As shown in Fig. 8(i), both the reconstructed leftmost and rightmost scatterer columns are discernible. In contrast, the reconstructed profiles of the two middle columns are obscure. Such a difference can also be seen in Fig. 8(d) and (j) although the high spatial frequency contents in the reconstructed leftmost and rightmost scatterer columns are partially filtered out due to the one-side layout of the transceiver array or a small array aperture size. Third, for small array aperture sizes, the reconstructed scatterer profiles when the transmitter array and the receiver array are placed on the same side of the inversion domain are worse than those when they are placed on two sides. However, this discrepancy almost disappears when θ_x becomes 88°. The reason for these phenomena has been explained in Section IV.

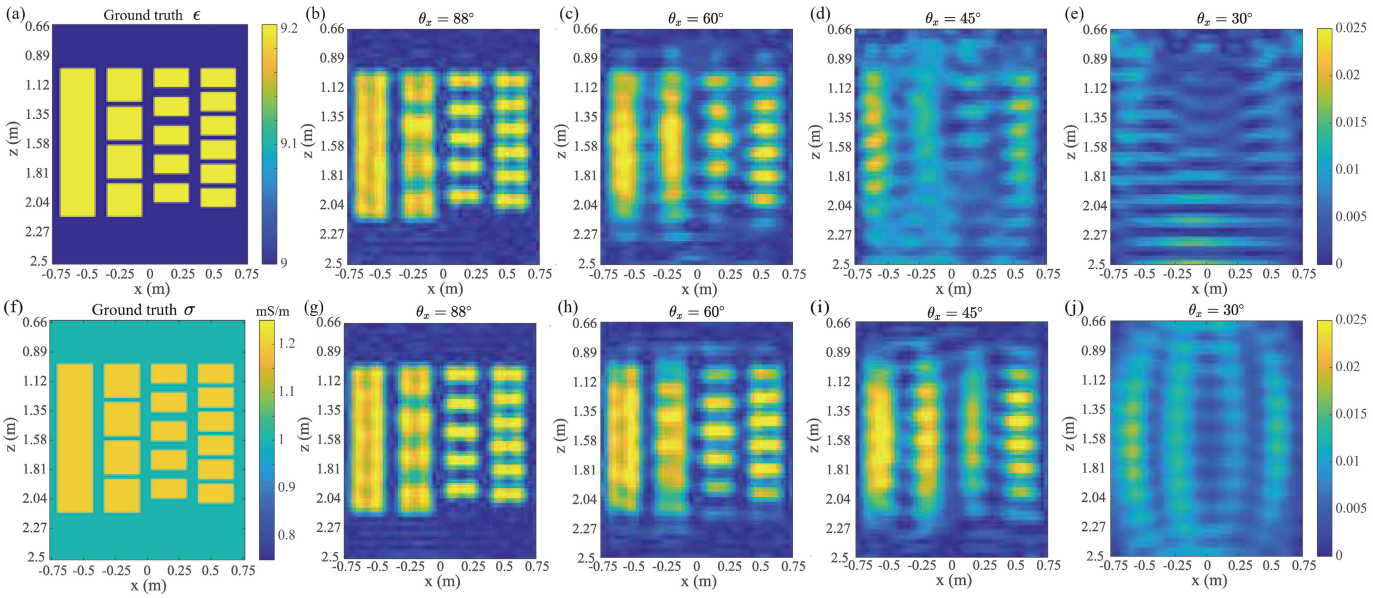

Fig. 8. Ground truth (a) permittivity profile and (f) conductivity profile of the 2-D scatterers and the reconstructed contrast moduli profiles for the four representative transceiver aperture sizes when the transmitter array and receiver array are placed on (b)–(e) the same side of the inversion domain and (g)–(j) two different sides.

VI. Conclusion and Future Work

In this work, for the first time, we have investigated how the transceiver array aperture size influences the reconstruction of 2-D scatterers embedded inside a planarly multilayered medium via both theoretical analysis and SVD analysis. Detailed mathematical formulas are derived to correlate the scattered electric field spectrum and the reconstructable spectrum of the scatterer when the multiple reflections and transmissions in layer boundaries are taken into account. The predicted results are verified by a series of numerical experiments. Compared with the results for the influence of transceiver array aperture size on the reconstruction of 2-D scatterers buried only in the subsurface region given in the previous work, both similarities and differences exist. The most significant similarity is the "lowpass" feature of the reconstructable spectra in the horizontal direction which actually is determined by the array aperture size. In contrast, the most significant difference is the vertical "bandstop" feature of the reconstructable spectrum of the scatterer embedded inside a planarly multilayered medium but the vertical "bandpass" feature of the reconstructable spectrum of the scatterer buried in the subsurface region. The "bandstop" spectrum is caused by the superposition of four spectral components which are generated by multiple reflections and transmissions in multiple layer boundaries and correspond to four different EM wave propagation pictures inside the inversion domain. In a half-space model, only one wave propagation picture remains since the multiple reflections vanish. Consequently, the "bandstop" feature degenerates into the "bandpass" feature.

There is a crucial issue that has not been addressed in this work. The influence of layer configurations, i.e., the dielectric parameters and the positions of layer boundaries, on the reconstructable spectra of 2-D scatterers embedded inside a planarly multilayered medium. The layer medium parameters and boundary positions mainly affect the reflection and transmission coefficients which are manifested by f_n in (8). Because we have assumed that all background layer parameters and boundary positions are fixed in this work, how the variation of f_n influences the reconstructable spectra is not studied. The future work will be focused on the computation of reconstructable spectra based on SVD for different spectral components and also the overall values when f_n takes different combinations. Other factors such as spatial sampling density of the transceivers for scattered electric fields, multifrequency data that have significant impacts on the reconstructable spectra [25], [26], [27], [28], [29], and the effect of the different aperture sizes of the transmitter array and the receiver array when they are placed on two different sides of the inversion domain will also be studied in the circumstance of multilayered media in our future work. Finally, it is worth mentioning the Born approximation adopted in this work. Both the theoretical and the numerical results presented in this work only adapt to weak EM scattering. Another future research branch is to remove the restriction of Born approximation and study how the array aperture size influences the inversion performance when the scatterers have high contrasts.

Appendix A

It is assumed the transmitter array is located inside the pth layer, i.e., $z_{p-1} < z_s < z_p$, the receiver array is located inside the qth layer, i.e., $z_{q-1} < z_r < z_q$, and the inhomogeneous scatterers are located inside the mth layer, i.e., $z_{m-1} < z < z_m$. Based on [30, Eq. (28)], the voltage at a certain field point (x, z) inside the mth layer excited by a current source in the

pth layer is

$$V_i^h(z) = \frac{Z_p^h}{2}\left[E_{0p}^h + \frac{1}{D_p^h}\left(\overrightarrow{\Gamma}_p^h\ E_{1p}^h + \overleftarrow{\Gamma}_p^h\ E_{2p}^h + \overrightarrow{\Gamma}_p^h \overleftarrow{\Gamma}_p^h\ (E_{3p}^h + E_{4p}^h)\right)\right] \tag{A1}$$

if $p = m$, and

$$V_i^h(z) = \frac{V_i^h(z_p)}{1 + \overrightarrow{\Gamma}_m^h\ e^{-j2k_{zm}d_m}} \prod_{i=p+1}^{m-1} \frac{\left(1 + \overrightarrow{\Gamma}_i^h\right) e^{-jk_{zi}d_i}}{1 + \overrightarrow{\Gamma}_i^h\ e^{-j2k_{zi}d_i}} \times e^{jk_{zm}(z - z_{m-1})}\left[1 + \overrightarrow{\Gamma}_m^h\ e^{-j2k_{zm}(z_m - z)}\right] \tag{A2}$$

if $p < m$, and

$$V_i^h(z) = \frac{V_i^h(z_{p-1})}{1 + \overleftarrow{\Gamma}_m^h\ e^{-j2k_{zm}d_m}} \prod_{i=m}^{p-2} \frac{\left(1 + \overleftarrow{\Gamma}_i^h\right) e^{-jk_{zi}d_i}}{1 + \overleftarrow{\Gamma}_i^h\ e^{-j2k_{zi}d_i}} \times e^{jk_{zm}(z_m - z)}\left[1 + \overleftarrow{\Gamma}_m^h\ e^{-j2k_{zm}(z - z_{m-1})}\right] \tag{A3}$$

if $p > m$. Note that $V_i^h(z_p)$ in (A2) and $V_i^h(z_{p-1})$ in (A3) are evaluated using (A1). The subscript of V_i^h denotes the current in the transmission line while i in the product is just an index. The mathematical expressions of Z_p^h, E_{0p}^h, D_p^h, E_{1p}^h, E_{2p}^h, E_{3p}^h, E_{4p}^h, $\overleftarrow{\Gamma}_m^h$, and $\overrightarrow{\Gamma}_m^h$ can be found in [34, Section V]. $d_i = z_i - z_{i-1}$ represents the thickness of the ith layer. In addition, $k_{zi}^2 + k_x^2 = k_i^2 = \epsilon_b^i k_0^2$ holds with k_0 being the wavenumber in free space. In addition, it is understood that the products in (A2) and (A3) are set to be one if the lower limit exceeds the upper limit.

Appendix B

The excitation source of each transmitter is assumed to be an infinitesimal dipole with the unit current moment. Therefore, its current density $J_y(\boldsymbol{\rho}_s)$ is one. Based on the expression of V_i^h given in Appendix A, when the transmitter array and the receiver array are located on the same side of the mth layer with $p < m$ and $q < m$, we have

$$V_i^h(k_x, z_r, z) V_i^h(k_x', z, z_s) = \sum_{n=1}^{10} f_n^{(1)} \cdot I_n^{(1)} \tag{B1}$$

where

$$I_1^{(1)} = I_3^{(1)} = I_5^{(1)} = e^{-j(k_{zm}' + k_{zm})z} \tag{B2a}$$
$$I_2^{(1)} = I_4^{(1)} = e^{-j(k_{zm}' - k_{zm})z} \tag{B2b}$$
$$I_6^{(1)} = I_8^{(1)} = I_{10}^{(1)} = e^{j(k_{zm}' - k_{zm})z} \tag{B2c}$$
$$I_7^{(1)} = I_9^{(1)} = e^{j(k_{zm}' + k_{zm})z} \tag{B2d}$$

and

$$f_1^{(1)} = f_{m>q} \cdot f_{p<m}' \cdot e^{j(k_{zm}' + k_{zm})z_{m-1}} \tag{B3a}$$
$$f_2^{(1)} = f_{m>q} \cdot f_{p<m}' \cdot \frac{\overrightarrow{\Gamma}_m^h}{D_m^h} e^{j(k_{zm}' + k_{zm})z_{m-1} - j2k_{zm}z_m} \tag{B3b}$$
$$f_3^{(1)} = f_{m>q} \cdot f_{p<m}' \cdot \frac{\overleftarrow{\Gamma}_m^h}{D_m^h} e^{j(k_{zm}' + k_{zm})z_{m-1}} \tag{B3c}$$
$$f_4^{(1)} = f_{m>q} \cdot f_{p<m}' \cdot \frac{\overrightarrow{\Gamma}_m^h \overleftarrow{\Gamma}_m^h}{D_m^h} e^{j(k_{zm}' - k_{zm})z_{m-1} - j2k_{zm}d_m} \tag{B3d}$$
$$f_5^{(1)} = f_{m>q} \cdot f_{p<m}' \cdot \frac{\overrightarrow{\Gamma}_m^h \overleftarrow{\Gamma}_m^h}{D_m^h} e^{j(k_{zm}' + k_{zm})z_{m-1} - j2k_{zm}d_m} \tag{B3e}$$
$$f_6^{(1)} = f_{m>q} \cdot f_{p<m}' \cdot \overrightarrow{\Gamma}_m^{h'} e^{j(k_{zm}' + k_{zm})z_{m-1} - j2k_{zm}'z_m} \tag{B3f}$$
$$f_7^{(1)} = f_{m>q} \cdot f_{p<m}' \cdot \frac{\overrightarrow{\Gamma}_m^h \overrightarrow{\Gamma}_m^{h'}}{D_m^h} e^{-j(k_{zm}' + k_{zm})(z_m + d_m)} \tag{B3g}$$
$$f_8^{(1)} = f_{m>q} \cdot f_{p<m}' \cdot \frac{\overleftarrow{\Gamma}_m^h \overrightarrow{\Gamma}_m^{h'}}{D_m^h} e^{j(k_{zm}' + k_{zm})z_{m-1} - j2k_{zm}'z_m} \tag{B3h}$$
$$f_9^{(1)} = f_{m>q} \cdot f_{p<m}' \cdot \frac{\overrightarrow{\Gamma}_m^h \overleftarrow{\Gamma}_m^h \overrightarrow{\Gamma}_m^{h'}}{D_m^h} \cdot e^{j(k_{zm}' - k_{zm})z_{m-1} - j2k_{zm}'z_m - j2k_{zm}d_m} \tag{B3i}$$
$$f_{10}^{(1)} = f_{m>q} \cdot f_{p<m}' \cdot \frac{\overrightarrow{\Gamma}_m^h \overleftarrow{\Gamma}_m^h \overrightarrow{\Gamma}_m^{h'}}{D_m^h} \cdot e^{j(k_{zm}' + k_{zm})z_{m-1} - j2k_{zm}'z_m - j2k_{zm}d_m} \tag{B3j}$$

in which

$$D_m^h = 1 - \overrightarrow{\Gamma}_m^h \overleftarrow{\Gamma}_m^h\ e^{-j2k_{zm}d_m} \tag{B4a}$$

$$f_{p<m}' = \frac{\omega\mu_0}{2k_{zp}'} \times \frac{1}{1 + \overrightarrow{\Gamma}_m^{h'}\ e^{-j2k_{zm}'d_m}} \times \left\{ e^{-jk_{zp}'(z_p - z_s)} + \frac{1}{1 - \overrightarrow{\Gamma}_p^{h'} \overleftarrow{\Gamma}_p^{h'}\ e^{-j2k_{zp}'d_p}} \times \left[\overrightarrow{\Gamma}_p^{h'}\ e^{-jk_{zp}'(z_p - z_s)} + \overleftarrow{\Gamma}_p^{h'}\ e^{-jk_{zp}'(z_p + z_s - 2z_{p-1})} + \overrightarrow{\Gamma}_p^{h'} \overleftarrow{\Gamma}_p^{h'}\ e^{-jk_{zp}'(2d_p + z_p - z_s)} + \overrightarrow{\Gamma}_p^{h'} \overleftarrow{\Gamma}_p^{h'}\ e^{-jk_{zp}'(2d_p + z_s - z_p)} \right] \right\} \times \prod_{i=p+1}^{m-1} \frac{\left(1 + \overrightarrow{\Gamma}_i^{h'}\right) e^{-jk_{zi}'d_i}}{1 + \overrightarrow{\Gamma}_i^{h'}\ e^{-j2k_{zi}'d_i}} \tag{B4b}$$

$$f_{m>q} = \frac{\omega\mu_0}{2k_{zm}} \times \frac{1}{\left(1 + \overleftarrow{\Gamma}_q^h\ e^{-j2k_{zq}d_q}\right) e^{jk_{zq}(z_q - z_r)}} \times \left[1 + \overleftarrow{\Gamma}_q^h\ e^{-j2k_{zq}(z_r - z_{q-1})}\right] \times \prod_{i=q}^{m-2} \frac{\left(1 + \overleftarrow{\Gamma}_i^h\right) e^{-jk_{zi}d_i}}{1 + \overleftarrow{\Gamma}_i^h\ e^{-j2k_{zi}d_i}} \tag{B4c}$$

where $\overleftarrow{\Gamma}_i^h$ and $\overrightarrow{\Gamma}_i^h$ are the TE-mode left and right global reflection coefficients in the ith layer, respectively, $d_i = z_i - z_{i-1}$ is the thickness of the ith layer, and the superscript apostrophe means the EM wave is emitted from the source point at (x_s, z_s). Note that the definitions and derivations of all the variables used in (B3) and (B4) can be found in [34, Section V]. The coefficient $f_{p<m}'$ depicts the wave propagation from the source point at (x_s, z_s) in the pth layer to the mth layer with $p < m$. In contrast, the coefficient $f_{m>q}$ depicts the wave propagation from the mth layer to the receiver point at (x_r, z_r) in the qth layer with $m > q$.

Now, let us shift to the EM scattering scenario in which the transmitter array and the receiver array are located on two

sides of the scatterer inside the mth layer with $p < m < q$. In this situation, we have

$$V_i^h(k_x, z_r, z)V_i^h(k_x', z, z_s) = \sum_{n=1}^{10} f_n^{(2)} \cdot I_n^{(2)} \tag{B5}$$

where

$$I_1^{(2)} = I_2^{(2)} = I_4^{(2)} = e^{-j\left(k_{zm}'-k_{zm}\right)z} \tag{B6a}$$

$$I_3^{(2)} = I_5^{(2)} = e^{-j\left(k_{zm}'+k_{zm}\right)z} \tag{B6b}$$

$$I_6^{(2)} = I_7^{(2)} = I_9^{(2)} = e^{j\left(k_{zm}'+k_{zm}\right)z} \tag{B6c}$$

$$I_8^{(2)} = I_{10}^{(2)} = e^{j\left(k_{zm}'-k_{zm}\right)z} \tag{B6d}$$

and

$$f_1^{(2)} = f_{m<q} \cdot f_{p<m}' \cdot e^{jk_{zm}'z_{m-1}-jk_{zm}z_m} \tag{B7a}$$

$$f_2^{(2)} = f_{m<q} \cdot f_{p<m}' \cdot \frac{\overrightarrow{\Gamma}_m^h}{D_m^h} e^{jk_{zm}'z_{m-1}-jk_{zm}z_m} \tag{B7b}$$

$$f_3^{(2)} = f_{p<m}' \cdot \frac{\overleftarrow{\Gamma}_m^h}{D_m^h} e^{jk_{zm}'z_{m-1}-jk_{zm}(d_m-z_{m-1})} \tag{B7c}$$

$$f_4^{(2)} = f_{m<q} \cdot f_{p<m}' \cdot \frac{\overrightarrow{\Gamma}_m^h \overleftarrow{\Gamma}_m^h}{D_m^h} e^{jk_{zm}'z_{m-1}-jk_{zm}(z_m+2d_m)} \tag{B7d}$$

$$f_5^{(2)} = f_{m<q} \cdot f_{p<m}' \cdot \frac{\overrightarrow{\Gamma}_m^h \overleftarrow{\Gamma}_m^h}{D_m^h} e^{jk_{zm}'z_{m-1}-jk_{zm}(z_m-2z_{m-1})} \tag{B7e}$$

$$f_6^{(2)} = f_{m<q} \cdot f_{p<m}' \cdot \overrightarrow{\Gamma}_m^{h'} e^{jk_{zm}'z_{m-1}-jk_{zm}z_m-j2k_{zm}'z_m} \tag{B7f}$$

$$f_7^{(2)} = f_{m<q} \cdot f_{p<m}' \cdot \frac{\overrightarrow{\Gamma}_m^h \overrightarrow{\Gamma}_m^{h'}}{D_m^h} e^{jk_{zm}'(z_{m-1}-2z_m)-jk_{zm}z_m} \tag{B7g}$$

$$f_8^{(2)} = f_{m<q} \cdot f_{p<m}' \cdot \frac{\overleftarrow{\Gamma}_m^h \overrightarrow{\Gamma}_m^{h'}}{D_m^h} \cdot e^{jk_{zm}'(z_{m-1}-2z_m)-jk_{zm}(z_m-2z_{m-1})} \tag{B7h}$$

$$f_9^{(2)} = f_{m<q} \cdot f_{p<m}' \cdot \frac{\overrightarrow{\Gamma}_m^h \overleftarrow{\Gamma}_m^h \overrightarrow{\Gamma}_m^{h'}}{D_m^h} \cdot e^{jk_{zm}'z_{m-1}-j\left(2k_{zm}'+k_{zm}\right)z_m-j2k_{zm}d_m} \tag{B7i}$$

$$f_{10}^{(2)} = f_{m<q} \cdot f_{p<m}' \cdot \frac{\overrightarrow{\Gamma}_m^h \overleftarrow{\Gamma}_m^h \overrightarrow{\Gamma}_m^{h'}}{D_m^h} \cdot e^{jk_{zm}'(z_{m-1}-2z_m)-jk_{zm}(z_m-2z_{m-1})} \tag{B7j}$$

where

$$f_{m<q} = \frac{\omega\mu_0}{2k_{zm}} \times \frac{1}{\left(1+\overrightarrow{\Gamma}_q^h e^{-j2k_{zq}d_q}\right)e^{jk_{zq}(z_r-z_{q-1})}} \times \left[1+\overrightarrow{\Gamma}_q^h e^{-j2k_{zq}(z_q-z_r)}\right] \times \prod_{i=m+1}^{q-1} \frac{\left(1+\overrightarrow{\Gamma}_i^h\right)e^{-jk_{zi}d_i}}{1+\overrightarrow{\Gamma}_i^h e^{-j2k_{zi}d_i}} \tag{B8}$$

is the coefficient depicting the wave propagation from the mth layer to the receiver point at $(x_r,\ z_r)$ in the qth layer with $m < q$.

REFERENCES

[1] X. Chen, *Computational Methods for Electromagnetic Inverse Scattering*. Solaris South Tower, Singapore: Wiley, 2018.

[2] A. Tijhuis, "Iterative determination of permittivity and conductivity profiles of a dielectric slab in the time domain," *IEEE Trans. Antennas Propag.*, vol. AP-29, no. 2, pp. 239–245, Mar. 1981.

[3] A. Tijhuis and C. van der Worm, "Iterative approach to the frequency-domain solution of the inverse-scattering problem for an inhomogeneous lossless dielectric slab," *IEEE Trans. Antennas Propag.*, vol. AP-32, no. 7, pp. 711–716, Jul. 1984.

[4] G. A. Newman and D. L. Alumbaugh, "Three-dimensional massively parallel electromagnetic inversion—I. Theory," *Geophys. J. Int.*, vol. 128, no. 2, pp. 345–354, Feb. 1997.

[5] D. L. Alumbaugh and G. A. Newman, "Three-dimensional massively parallel electromagnetic inversion—II. Analysis of a crosswell electromagnetic experiment," *Geophys. J. Int.*, vol. 128, no. 2, pp. 355–363, Feb. 1997.

[6] Y. M. Wang and W. C. Chew, "An iterative solution of the two-dimensional electromagnetic inverse scattering problem," *Int. J. Imag. Syst. Technol.*, vol. 1, no. 1, pp. 100–108, 1989.

[7] W. C. Chew and Y. M. Wang, "Reconstruction of two-dimensional permittivity distribution using the distorted Born iterative method," *IEEE Trans. Med. Imag.*, vol. 9, no. 2, pp. 218–225, Jun. 1990.

[8] N. Zaiping, Y. Feng, Z. Yanwen, and Z. Yerong, "Variational Born iteration method and its applications to hybrid inversion," *IEEE Trans. Geosci. Remote Sens.*, vol. 38, no. 4, pp. 1709–1715, Jul. 2000.

[9] P. M. V. D. Berg and R. E. Kleinman, "A contrast source inversion method," *Inverse Problems*, vol. 13, no. 6, pp. 1607–1620, Dec. 1997.

[10] P. M. V. D. Berg, A. L. V. Broekhoven, and A. Abubakar, "Extended contrast source inversion," *Inverse Problems*, vol. 15, no. 5, pp. 1325–1344, Oct. 1999.

[11] X. Chen, "Subspace-based optimization method for solving inverse-scattering problems," *IEEE Trans. Geosci. Remote Sens.*, vol. 48, no. 1, pp. 42–49, Jan. 2010.

[12] N. Zaiping and Z. Yerong, "Hybrid Born iterative method in low-frequency inverse scattering problem," *IEEE Trans. Geosci. Remote Sens.*, vol. 36, no. 3, pp. 749–753, May 1998.

[13] X. Ye et al., "Application of subspace-based distorted-Born iteration method in imaging biaxial anisotropic scatterer," *IEEE Trans. Comput. Imag.*, vol. 6, pp. 1486–1492, 2020.

[14] C. Yu, M. Yuan, and Q. H. Liu, "Reconstruction of 3D objects from multi-frequency experimental data with a fast DBIM-BCGS method," *Inverse Problems*, vol. 25, no. 2, pp. 1–24, Feb. 2009.

[15] J. Li, J. Zhuo, Z. Guan, F. Han, and Q. H. Liu, "3-D electromagnetic scattering and inverse scattering by magnetodielectric objects with arbitrary anisotropy in layered uniaxial media," *IEEE Trans. Antennas Propag.*, vol. 68, no. 2, pp. 1009–1022, Feb. 2020.

[16] Y. Sanghvi, Y. Kalepu, and U. K. Khankhoje, "Embedding deep learning in inverse scattering problems," *IEEE Trans. Comput. Imag.*, vol. 6, pp. 46–56, 2020.

[17] K. Agarwal, L. Pan, and X. Chen, "Subspace-based optimization method for reconstruction of 2-D complex anisotropic dielectric objects," *IEEE Trans. Microw. Theory Techn.*, vol. 58, no. 4, pp. 1065–1074, Apr. 2010.

[18] T. J. Cui, W. C. Chew, A. A. Aydiner, D. L. Wright, and D. V. Smith, "Detection of buried targets using a new enhanced very early time electromagnetic (VETEM) prototype system," *IEEE Trans. Geosci. Remote Sens.*, vol. 39, no. 12, pp. 2702–2712, Dec. 2001.

[19] R. Hong et al., "3-D MRI-based electrical properties tomography using the volume integral equation method," *IEEE Trans. Microw. Theory Techn.*, vol. 65, no. 12, pp. 4802–4811, Dec. 2017.

[20] W. Rodi and R. L. Mackie, "Nonlinear conjugate gradients algorithm for 2-D magnetotelluric inversion," *Geophysics*, vol. 66, no. 1, pp. 174–187, 2001.

[21] D. Avdeev and A. Avdeeva, "3D magnetotelluric inversion using a limited-memory quasi-Newton optimization," *Geophysics*, vol. 74, no. 3, pp. F45–F57, May 2009.

[22] J. Xie et al., "3-D magnetotelluric inversion and application using the edge-based finite element with hexahedral mesh," *IEEE Trans. Geosci. Remote Sens.*, vol. 60, 2022, Art. no. 4503011.

[23] W. Siripunvaraporn and G. Egbert, "Data space conjugate gradient inversion for 2-D magnetotelluric data," *Geophys. J. Int.*, vol. 170, no. 3, pp. 986–994, Sep. 2007.

[24] H. Jahandari and C. G. Farquharson, "3-D minimum-structure inversion of magnetotelluric data using the finite-element method and tetrahedral grids," *Geophys. J. Int.*, vol. 211, no. 2, pp. 1189–1205, Nov. 2017.

[25] G. Leone and F. Soldovieri, "Analysis of the distorted Born approximation for subsurface reconstruction: Truncation and uncertainties effects," *IEEE Trans. Geosci. Remote Sens.*, vol. 41, no. 1, pp. 66–74, Jan. 2003.

[26] R. Persico, R. Bernini, and F. Soldovieri, "The role of the measurement configuration in inverse scattering from buried objects under the Born approximation," *IEEE Trans. Antennas Propag.*, vol. 53, no. 6, pp. 1875–1887, Jun. 2005.

[27] O. M. Bucci, L. Crocco, T. Isernia, and V. Pascazio, "Inverse scattering problems with multifrequency data: Reconstruction capabilities and solution strategies," *IEEE Trans. Geosci. Remote Sens.*, vol. 38, no. 4, pp. 1749–1756, Jul. 2000.

[28] R. Persico, F. Soldovieri, and G. Leone, "A microwave tomographic imaging approach for multibistatic configuration: The choice of the frequency step," *IEEE Trans. Instrum. Meas.*, vol. 55, no. 6, pp. 1926–1934, Dec. 2006.

[29] F. Soldovieri, R. Persico, and G. Leone, "Effect of source and receiver radiation characteristics in subsurface prospecting within the distorted Born approximation," *Radio Sci.*, vol. 40, no. 3, pp. 1–13, Jun. 2005.

[30] K. A. Michalski and J. R. Mosig, "Multilayered media green's functions in integral equation formulations," *IEEE Trans. Antennas Propag.*, vol. 45, no. 3, pp. 508–519, Mar. 1997.

[31] M. Bertero and P. Boccacci, *Introduction to Inverse Problems in Imaging*. Boca Raton, FL, USA: CRC Press, 1998.

[32] S. Twomey, *Introduction to the Mathematics of Inversion in Remote Sensing and Indirect Measurements*. New York, NY, USA: Dover, 1977.

[33] F. Han, J. Zhuo, N. Liu, Y. Liu, H. Liu, and Q. H. Liu, "Fast solution of electromagnetic scattering for 3-D inhomogeneous anisotropic objects embedded in layered uniaxial media by the BCGS-FFT method," *IEEE Trans. Antennas Propag.*, vol. 67, no. 3, pp. 1748–1759, Mar. 2019.

[34] F. Han, J. Zhuo, S. Lu, J. Wang, and Q. H. Liu, "Explicit semianalytical expressions of sensitivity matrices for the reconstruction of 1-D planarly layered TI media illuminated by 3-D sources," *IEEE Trans. Antennas Propag.*, vol. 70, no. 2, pp. 1547–1552, Feb. 2022.

Sijia Ma received the B.S. degree in electronic information science and technologies from Shaanxi Normal University, Xi'an, China, in 2021. She is currently pursuing the master's degree with Xiamen University, Xiamen, China.

Her research interests include electromagnetic inverse scattering and antenna array configuration for electromagnetic full-wave inversion.

Kemeng Tao received the B.E. degree in electronic information engineering from Xiangtan University, Xiangtan, China, in 2020. She is currently pursuing the master's degree with Xiamen University, Xiamen, China.

Her research interests include electromagnetic inverse scattering and antenna array configuration for electromagnetic full-wave inversion.

Feng Han (Senior Member, IEEE) received the B.S. degree in electronic science from Beijing Normal University, Beijing, China, in 2003, the M.S. degree in geophysics from Peking University, Beijing, in 2006, and the Ph.D. degree in electrical engineering from Duke University, Durham, NC, USA, in 2011.

From 2011 to 2015, he was a Software Engineer at Wavenovation, Inc., Xiamen, China. In July 2015, he joined the Institute of Electromagnetics and Acoustics, Xiamen University, Xiamen, as an Assistant Professor and was promoted to Associate Professor there in 2020. In October 2023, he joined the School of Computing and Information Technology, Great Bay University, Dongguan, China, as an Associate Professor. He has published over 50 articles in refereed journals. His research interests include electromagnetic scattering and inverse scattering in complex media, multiparametric and multidimensional hybrid electromagnetic full-wave inversion, fast electromagnetic full-wave inversion based on scientific machine learning, configuration of the antenna array for electromagnetic inverse problems, and geophysical electromagnetic exploration and inversion.